Defect Clusters and Superstructures of Zr^{4+} Dissolved $Ni_{1-x}O$

J. Chen and P. Shen[1]

Institute of Materials Science and Engineering, National Sun Yat-sen University, Kaohsiung, Taiwan

$Ni_{1-x}O$ ($x < 0.001$) powders, pure and mixed with pure ZrO_2 or yttria–partially stabilized zirconia (Y-PSZ), were sintered and then annealed at 1573 and 1873 K for up to 300 h to investigate the dopant dependence of defect clustering in the $Ni_{1-x}O$ lattice. Transmission electron microscopic observations coupled with energy X-ray analysis indicated that the dissolution of Zr^{4+} (ca. 2.0 mol% with or without co-dopant $Y^{3+} < 0.3$ mol%) but not Ni^{3+} caused defect clustering, which was more rapid at 1873 than 1573 K and which preferred to nucleate at interfaces and dislocations. The paracrystalline distribution of defects was found to be nearly 3.5 and 2.5 times the lattice parameter of $Ni_{1-x}O$ for Zr-doped and (Zr,Y)-codoped $Ni_{1-x}O$, respectively. The predominantly dissolved Zr^{4+} cations, in octahedral sites with charge- and volume-compensating nickel and oxygen vacancies (i.e., $Zr^{oct}\square_nO_{6-m}\square_m$), could create local domains in which Ni^{3+} should be expelled and, thus, in the vicinity the paracrystalline state and then the spinel Ni_3O_4 could precipitate in local domains. The spinelloid, a superstructure of spinel with a relatively high Zr^{4+} content (ca. 3.5 mol%), appeared only for the $Ni_{1-x}O$ particles located at Y-PSZ grain boundaries. © 1998 Academic Press

1. INTRODUCTION

Wüstite ($Fe_{1-x}O$) is an oxide with the rock-salt structure that shows a considerable degree of nonstoichiometry, extending to $x = 0.15$ at high temperatures (1), and defect clustering and ordering (2–21). The first indication of defect clustering was the detection of tetrahedral interstitials by powder neutron diffraction measurements on samples quenched to room temperature (2). The tetrahedral interstitials were later found to be Fe^{3+} by Mössbauer measurements (3). Lattice energy calculations (4–8) indicated defect cluster stability relative to unassociated point defects, and the most stable clusters are built from a basic unit of four octahedral iron vacancies tetrahedrally coordinated about one iron interstitial (i.e., 4:1 cluster). Aggregation of 4:1 clusters is expected because the creation of interstitials in an environment of four vacancies is highly favorable energetically. Neutron diffraction of $Fe_{1-x}O$ at high temperatures (9–12)

indeed showed the presence of such clusters, and in general, the vacancy to interstitial ratio, ρ, increases as the temperature or Fe content decreases (11).

Long range ordering of defect clusters in $Fe_{1-x}O$ was known to cause the formation of spinel phase, P″ and P‴ (13, 14). In addition, the P′ phase, originally interpreted as a $2.6 \times 2.6 \times 2.6$ supercell of wüstite (15), gave diffuse X-ray scattering patterns consistent with a paracrystalline array of defect clusters inhomogeneously embedded in the rock-salt substructure (16, 17). The paracrystalline distribution is such that the spacing between defect clusters tends to be maintained fairly constant but relative lateral translations may occur more variably, hence negligible diffraction intensity beyond first order. (The paracrystalline model for the P′ structure is different from the structure imaged with high resolution transmission electron microscopy (HRTEM) (18, 19). The latter appears to be a stacking-disordered noncubic structure probably due to a higher x ($x = 0.08$) than Ref. (16) ($x = 0.057$). In fact, $Fe_{1-x}O$ with $x = 0.098$ has been suggested to have incommensurate structure with three-dimensional modulation (9, 20).) When the lateral translations of the P′ phase are suppressed, the superlattice P″ phase appears (15). The P″ phase was suggested to consist of clusters composed of 10 vacancies and 4 interstitial ferric irons, according to computer simulation of the HRTEM image (21).

In contrast to wüstite, busenite ($Ni_{1-x}O$), also with the rock salt structure, has very small x (ca. 0.001 at 1773 K (22)) and the occurrence of defect clustering is uncertain whether from a theoretical point of view (6, 23) or based on experimental results (24–28). There is, however, clearer experimental evidence of defect clustering in cation-doped $Ni_{1-x}O$. For example, (Zr,Y)-codoped $Ni_{1-x}O$ gave diffraction patterns consistent with a paracrystalline ordered state which developed subsequently into a spinel structure upon annealing at 1573 K (29).

The motivation of this study was to clarify the dopant (Ni^{3+}, Zr^{4+}, Y^{3+}) dependence of defect clustering in $Ni_{1-x}O$ and to identify the superstructures, if any, for $Ni_{1-x}O$-derived spinel. The $Ni_{1-x}O$ polycrystals and two composites, $Ni_{1-x}O/ZrO_2$ and $Ni_{1-x}O/Y$-PSZ, were annealed at two temperatures (1573 and 1873 K) and resultant phase changes characterized by TEM.

2. EXPERIMENTAL

The $Ni(CH_3COO)_2$ powders (Janssen) and those added with ZrO_2 (Gredman) or yttria–partially stabilized zirconia (Y-PSZ, with 6 mol % Y_2O_3 and containing tetragonal (t) precipitates within a cubic (c) matrix, Toyo Soda) powders were ultrasonically vibrated in distilled water to prevent soft agglomeration, stirred for homogeneity, and calcined at 1073 K for 5 h. The powder batches thus formed include $Ni_{1-x}O$, $Ni_{1-x}O/ZrO_2$ (5:1 and 9:1 molar ratios, denoted as N_5Z_1 and N_9Z_1), and $Ni_{1-x}O/Y$-PSZ (1:9 molar ratio, designated as $N_1Y_{0.5}Z_{8.5}$). The powder batches were then die-pressed at 60 MPa to form pellets about 10 mm in diameter, followed by sintering at 1873 K for 10 h and cooling in an open air furnace ($PO_2 = 0.2$ atm). The $N_1Y_{0.5}Z_{8.5}$ specimen was also sintered for a shorter time period (1 h at 1873 K) in order to study the early stage of defect clustering. The sintered specimens were further annealed at 1573 and 1873 K for up to 300 h and cooled in the furnace.

X-ray diffraction (XRD, Cu$K\alpha$, 40 kV, 30 mA) at 0.02° per step and 2 s per step was used to identify the phases of the fired specimens. Thin sections (about 10–20 μm in thickness) of the samples were argon-ion milled to electron transparency and studied by TEM, using a JEOL 3010 instrument operating at 300 kV for imaging and 200 kV for energy dispersive X-ray (EDX) analysis. The EDX analysis was performed using L shell counts for Zr and Y and K shell counts for Ni, and the principle of ratio method without absorption correction (30). The error was estimated to be within ± 5%.

3. RESULTS

3.1. $Ni_{1-x}O$ Polycrystals

The $Ni_{1-x}O$ polycrystals appeared dark green to the naked eye. A higher annealing temperature (1873 vs 1573 K) caused a darker color of the specimen, because of a higher Ni^{3+} content in $Ni_{1-x}O$ according to Ref. (22). Still the Ni^{3+} content was not high enough to cause phase change of $Ni_{1-x}O$, as indicated by electron diffraction of the sample aged at 1873 K for 300 h.

3.2. $Ni_{1-x}O/ZrO_2$ Composites

XRD and TEM indicated the N_5Z_1 and N_9Z_1 composites fired at 1573 or 1873 K contained the monoclinic (m) ZrO_2 particles in the $Ni_{1-x}O$ matrix which was dissolved with ca. 2 mol% Zr according to EDX analysis. This dopant level was adequate for defect clustering in the $Ni_{1-x}O$ matrix when aging was conducted at a high enough temperature. In fact, the Zr-dissolved $Ni_{1-x}O$ remained as a rock salt structure when aged at 1573 K for 300 h, but showed paracrystalline lattice at 1873 K for 100 h, as indicated by sideband
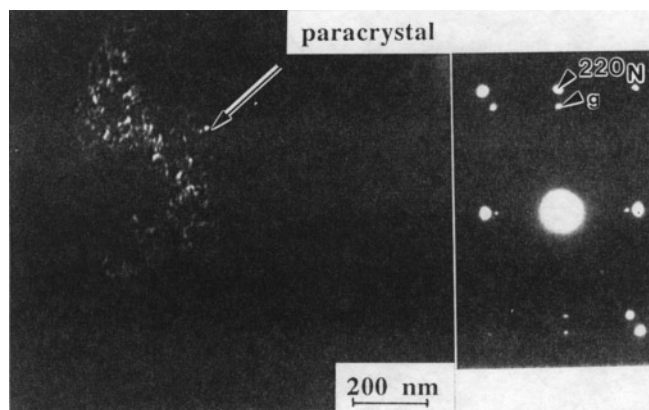

FIG. 1. Dark field image (DFI) and SAD pattern (Z = [112]) of $Ni_{1-x}O$ (N) derived paracrystalline lattice, using sideband spot (g, arrow) with a unit ca. 1/3.5 times the lattice parameter of $Ni_{1-x}O$, N_9Z_1 composite annealed at 1873 K for 100 h.

diffraction spots of $Ni_{1-x}O$, with a unit ca. 1/3.5 times the lattice parameter (a_o) in the reciprocal space (Fig. 1). The SAD pattern of Fig. 1 shows that the intensity of the sideband spots on the low angle side of the Bragg peaks are higher than those on the high-angle side, analogous to the case of X-ray diffraction pattern for quenched $Fe_{1-x}O$ with $x = 0.057$ (16, 17). However, different intensity distribution of sideband spots was also observed (e.g., Fig. 2). Presumably the intensity of the central Bragg peak relative to the incommensurate sideband peaks is affected by both the fraction of the crystal which is defect free and also the size of the individual defect clusters of a paracrystalline lattice (17). The lattice image showed a disordered region presumably due to a paracrystalline-like array of defect clusters, which was partially replaced by an imperfect spinel phase having parallel epitaxy with respect to the $Ni_{1-x}O$ matrix (Fig. 2). The spinel phase was also found to form platelets with {100} habit plane (Fig. 3). Similarly to the case of $NiAl_2O_4$ spinel precipitation from Al-doped $Ni_{1-x}O$ (31), the present spinel platelets were likely formed by nucleation at dislocations, known to have line vector parallel to the ⟨100⟩ direction for pure nickel oxide (32). It is noteworthy that the spinel platelets have {110} planar antiphase domain boundary as for $NiAl_2O_4$ spinel (31).

3.3. $Ni_{1-x}O/Y$-PSZ Composite
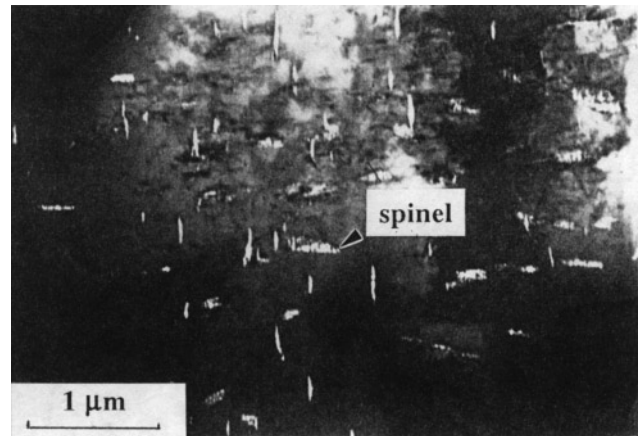
According to our previous study of this composite (29), the (Zr,Y)-codoped $Ni_{1-x}O$ occurred as intra- and inter-granular particles within the (c + t)-ZrO_2 matrix and the particles remained in the rock salt structure when aged at 1573 K within 100 h. In contrast, a much shorter aging duration (1 h) at a higher temperature (1873 K) in this study caused rapid formation of the paracrystalline state and spinel phase as represented by an intragranular $Ni_{1-x}O$
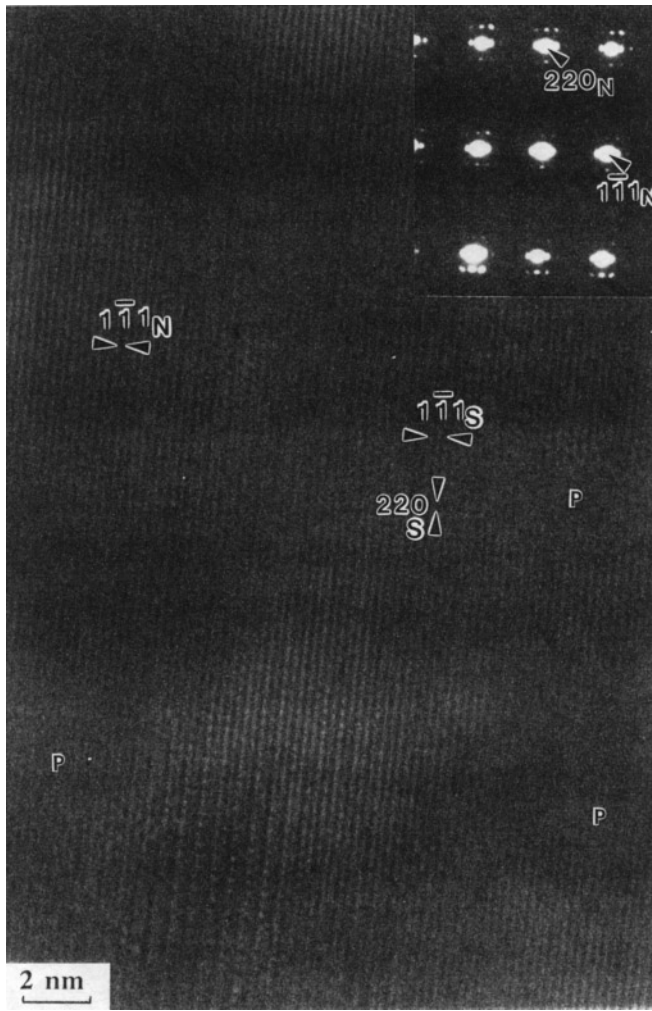
FIG. 2. Lattice image of disordered region, presumably due to paracrystalline-like (P) distribution of defect clusters, and the spinel (S) phase having parallel epitaxy with respect to the $Ni_{1-x}O$ (N) matrix; note the lattice fringes of the spinel phase are slightly corrugated and the spinel diffraction spots are rather weak compared to the paracrystalline sideband spots in the inset SAD pattern ([112] zone axis), the same specimen as Fig. 1.

FIG. 3. DFI of spinel platelets with {110} type antiphase domain boundaries, preferentially nucleated at dislocations in the $Ni_{1-x}O$ matrix, N_5Z_1 composite annealed at 1873 K for 100 h.

particle in Fig. 4a. The paracrystalline distribution of defect clusters in the (Zr,Y)-codoped $Ni_{1-x}O$ particles was found to be ca. 2.5 times the lattice parameter of $Ni_{1-x}O$, considerably smaller than in the case of Zr-doped $Ni_{1-x}O$. The intergranular $Ni_{1-x}O$ particles of the same sample showed that the spinel phase was predominantly formed next to the pore and contained wavelike variations giving rise to modulating sideband spots (Fig. 4b).

After a longer firing at 1873 K for 110 h, 10 h sintering and 100 h aging, the paracrystalline distribution spacing of defect clusters remained the same (Fig. 5a) but the spinel phase was found to develop into larger patches at the $Ni_{1-x}O$/Y-PSZ interface (Fig. 5b). Prolonged aging at 1873 K for 300 h was found to cause considerable growth of the spinel precipitates from an intragranular $Ni_{1-x}O$ par-

ticle (Fig. 6). The spinel precipitate has a zigzag {100} habit plane with {111} facets (Fig. 6), presumably due to nucleation at $Ni_{1-x}O$/Y-PSZ interface and then growth along the $\langle 100 \rangle$ dislocation of the $Ni_{1-x}O$. Note that the intragranular $Ni_{1-x}O$ particles in Fig. 6 have reached parallel epitaxial orientation with respect to the Y-PSZ grain, via a Brownian-type rotation of the particle (33), and the coexistence of $Ni_{1-x}O$, spinel, and Y-PSZ in epitaxial orientation causes a Moiré fringe. The epitaxial spinel patches could separate from the $Ni_{1-x}O$ particle when the Y-PSZ grain boundary moved across the particle, as shown in Fig. 7.

Prolonged aging for 300 h at 1873 K caused further ordering of the spinel phase in the $Ni_{1-x}O$ particle located at Y-PSZ grain boundaries (Fig. 8). The SAD pattern taken from two of the ordered patches (labeled as 1 and 2 in Fig. 8) showed superlattice spots spaced $\frac{1}{4}$ the fundamental $Ni_{1-x}O$ (200) spots in two reciprocal $\langle 100 \rangle$ directions. A single variant was used to take SAD patterns in the zone axes [001], [011], and [111] (Fig. 9a, b, and c, respectively) in order to construct the reciprocal lattice (r.p.l.) in Section 4.4. The spinel-derived phase contained planar defects parallel to a specific $\{110\}_N$ plane of the $Ni_{1-x}O$ (N) sublattice as shown edge-on in the [111] zone axis in Fig. 10, consistent with diffraction streaks along the reciprocal $[\bar{1}10]_N$ direction (Fig. 9c).

EDX concentration profiles across interphase interfaces for a number of intragranular $Ni_{1-x}O$ particles in the composite fired at 1873 K for 1 h vs 300 h indicated that solid solubility has been reached within 1 h. The composition was rather uniform for the zirconia matrix (ca. 2.5 mol% Ni and 6.3 mol% Y) and the $Ni_{1-x}O$ particles (ca. 2.0 mol% Zr and very small content of Y (< 0.3 mol%)) regardless of the presence of paracrystalline lattice and spinel patches. (A nearly null Y content in $Ni_{1-x}O$ is in accordance with the NiO/Y_2O_3 phase diagram (34). The NiO phase in directionally solidified eutectic (DSE) NiO/ZrO_2 (CaO) lamellae,
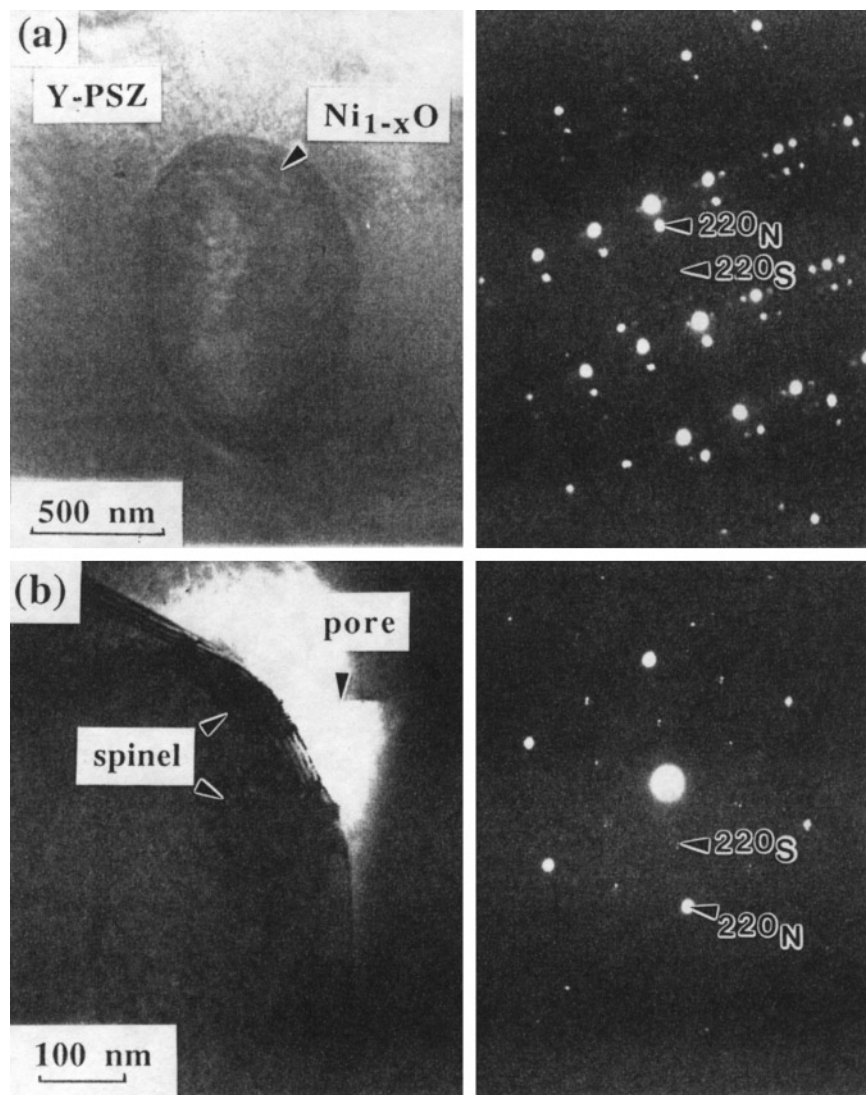
FIG. 4. Bright field image (BFI) and inset SAD pattern of (a) an intragranular $Ni_{1-x}O$ particle containing spinel phase and paracrystalline lattice with a real space spacing ca. 2.5 times the lattice parameter of $Ni_{1-x}O$ and (b) an intergranular $Ni_{1-x}O$ particle which has well developed spinel patches (with modulation sideband spots) next to the pore, the $N_1Y_{0.5}Z_{8.5}$ composite shortly sintered at 1873 K for 1 h.

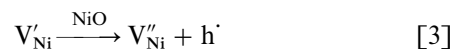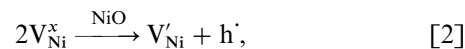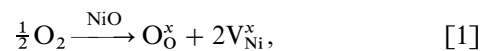however, has been reported to contain null Zr content (35), presumably due to a flat and low-energy $(111)_{NiO}/(100)_{ZrO2}$ interface which prohibited successful jump of atoms, i.e., interface-controlled.) The spinel-derived phase in the intergranular $Ni_{1-x}O$ particles has a relatively high Zr content (ca. 3.5 mol%) but a similar dopant level of Y (< 0.3 mol%) in comparison with the spinel phase in the intragranular $Ni_{1-x}O$ particles.

4. DISCUSSION

### 4.1. Thermal and Surface Effects on the Ni^{3+}/Ni^{2+} Ratio of $Ni_{1-x}O$ Polycrystals

Ideal nickel monoxide has cations and anions in the octahedral site. Point defects are introduced by reactions with the oxygens surrounding the $Ni_{1-x}O$ crystal, which are usually written (36, 37) as

$$\frac{1}{2}O_2 \xrightarrow{\text{NiO}} O_O^x + 2V_{Ni}^x, \qquad [1]$$

$$2V_{Ni}^x \xrightarrow{\text{NiO}} V_{Ni}' + h^\cdot, \qquad [2]$$

$$V_{Ni}' \xrightarrow{\text{NiO}} V_{Ni}'' + h^\cdot \qquad [3]$$
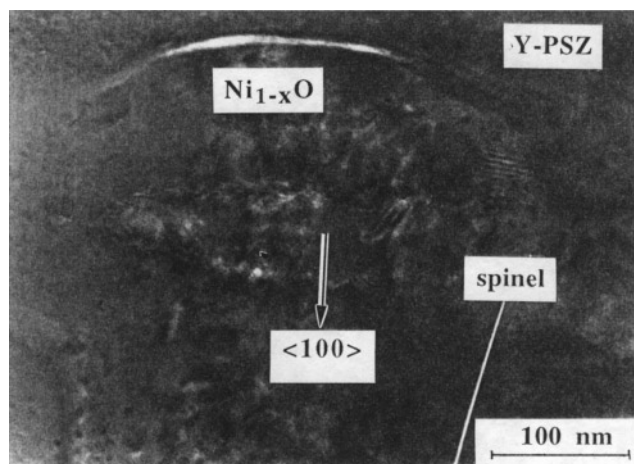
in Kröger–Vink notation (38). Under specified oxygen partial pressure, the $[V_{Ni}'']/[V_{Ni}']$ ratio is less than 1 but increases with increased temperature over the temperature
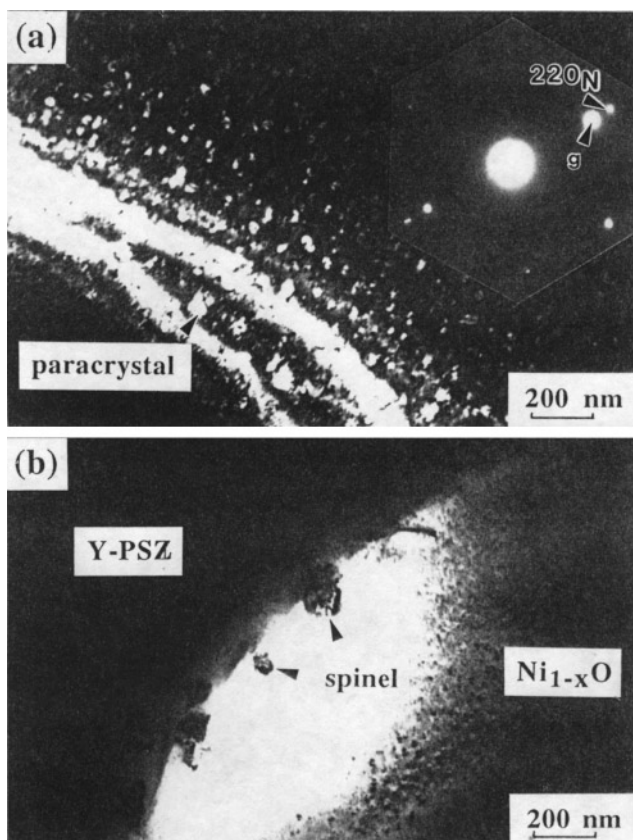
FIG. 5. (a) DFI (using sideband spot 1/2.5 times the lattice parameter of Ni$_{1-x}$O, denoted as g) and inset SAD pattern (near [111] zone axis) of the paracrystalline lattice in the Ni$_{1-x}$O matrix. (b) DFI of relatively large spinel patches at the Ni$_{1-x}$O/Y-PSZ interface, the N$_1$Y$_{0.5}$Z$_{8.5}$ composite fired at 1873 K for 110 h, 10 h sintering and 100 h annealing.


FIG. 6. BFI of a zigzag {100} habit plane of the spinel precipitate in an intragranular Ni$_{1-x}$O particle which reached parallel epitaxy with the Y-PSZ matrix (see text) when the N$_1$Y$_{0.5}$Z$_{8.5}$ composite was fired at 1873 K for 310 h, 10 h sintering and 300 h annealing. The moiré fringes are due to the superimposed Ni$_{1-x}$O, spinel, and ZrO$_2$ in epitaxial orientation.

range 1273–1973 K because V$''_{Ni}$ moves with a smaller activation enthalpy than V$'_{Ni}$ (39). According to Atkinson et al. (37), the nature of "singly charged" nickel vacancies in Ni$_{1-x}$O is in fact a combination of an electron hole with a conventional Ni vacancy. Presumably, hole localization results in a bound pair of point defects on the Ni sites: V$''_{Ni}$ + Ni^{3+}Ni$^{.}$. The electron hole may also be captured by a Ni^{2+} ion in the form of Ni$_i^{...}$, but the Ni$_{Ni}$ dominates over Ni$_i^{...}$ because of the high octahedral site preference energy of the Ni^{3+} dopant (40). In general, a higher temperature oxidation through Eqs. [1]–[3] is expected to increase the Ni^{3+}/Ni^{2+} ratio. A pronounced effect of temperature on the increase of Ni^{3+} concentration (> 0.1%) is indeed indicated by the appearance of a dark green color in the fired Ni$_{1-x}$O (22).

In addition to the temperature effect, theoretical calculation indicated that nickel vacancy concentration increases by a factor of about 40 over the bulk value for the (211)/[011] twist grain boundary of Ni$_{1-x}$O at 1000 K (41). A high Ni^{3+}/Ni^{2+} ratio is also expected for the free surface

of the Ni$_{1-x}$O particles as far as the reactions [1]–[3] are of concern. In this connection, the near-surface layers of Fe$_2$O$_3$ (42) and CoO (43) indeed have much higher deviations from stoichiometry and higher defect concentrations than the bulk.

In spite of the thermal and surface effects, the Ni^{3+}/Ni^{2+} ratio of the present Ni$_{1-x}$O polycrystals was still not high enough to cause appreciable defect clustering or the formation of the superstructures.

4.2. Effect of Dopants on Defect Clustering of Ni$_{1-x}$O

(a) Interstitial-tetrahedral dopants. Theoretical calculations (40) indicated interstitial-tetrahedral dopants can stabilize 4:1 defect clusters in 3d transition metal monoxide, e.g., Mn^{3+}- and Fe^{3+}-based 4:1 clusters in Co$_{1-x}$O and Ni$_{1-x}$O. The formation of the paracrystalline state of defect clusters and then spinel precipitates in Al-doped Ni$_{1-x}$O was also suggested to be triggered by change in defect type from clusters with octahedral Al to those with interstitial-tetrahedral Al on decreasing temperature (31):

$$\text{Al}^{.}_{Ni} + 2\text{V}''_{Ni} + 2\text{Ni}^{.}_{Ni} \rightarrow [\text{Al}_i^{...} + 4\text{V}''_{Ni} + 4\text{Ni}^{.}_{Ni}]. \quad [4]$$
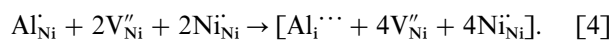
(b) Substitutional-octahedral dopant Zr^{4+}. The existence of Zr$^{4+}\square_4$ clusters, i.e., four octahedral nickel vacancies ($\square$) tetrahedrally coordinated about one Zr^{4+} interstitial, in Ni$_{1-x}$O is, however, fully questionable. In ideal c-ZrO$_2$ (CaF$_2$ structure), the environment of Zr^{4+} is of 8 oxygen atoms ([ZrO$_8$] groups) because of the larger radius of Zr^{4+} (0.084 nm in coordination number of 8 according to Ref. (44)) in presence of oxygen. In fact, a larger
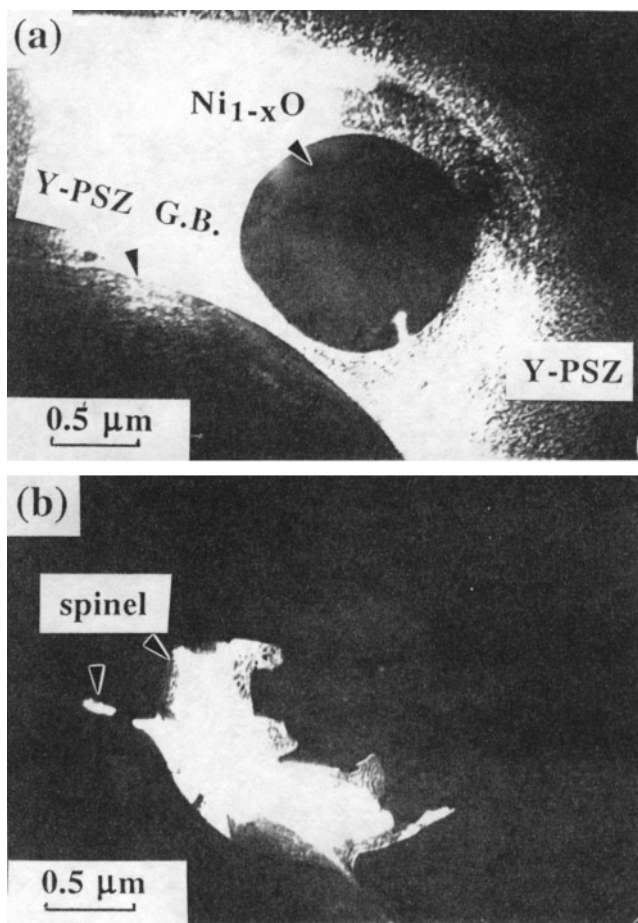
FIG. 7. Nonepitaxy $Ni_{1-x}O$ particle just detached from Y-PSZ grain boundary (G.B.). (a) DFI of the Y-PSZ grain with imbedded $Ni_{1-x}O$ particle; (b) DFI of the punched-off spinel patches (same specimen as Fig. 5).
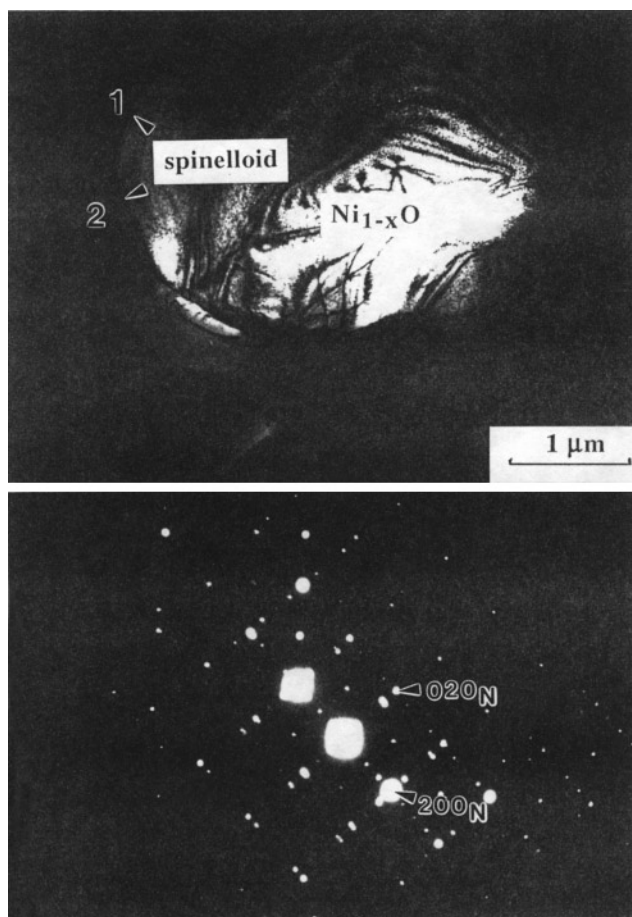
FIG. 8. (a) BFI and (b) SAD pattern of spinel-derived variants (labeled as 1 and 2) in an intergranular $Ni_{1-x}O$ particle (same specimen as Fig. 6).

room-temperature lattice parameter for Zr-dissolved $Ni_{1-x}O$ ($a_o = 0.4198$ nm (45)) than pure $Ni_{1-x}O$ ($a_o = 0.4177$ nm, JCPDS File 4-0835) can be explained by the sole presence of Zr^{4+} in octahedral sites in view of a larger ionic size of Zr^{4+} (0.072 nm) than Ni^{2+} (0.069 nm) in coordination number of 6 (44). These octahedral (oct) sites can easily accommodate a sufficient space, mainly in the presence of additional vacancies: $Zr^{oct}\square_nO_6$ with $n = 1$ to 6. The charge balance perturbed by the dissolution of Zr^{4+} is expected to create $Zr^{..}_{Ni}$ (i.e., in the octahedral substitution site), charge-compensated by V''_{Ni} or $[V''_{Ni} + Ni^{.}_{Ni}]$ through the following reactions:

$$ZrO_2 \xrightarrow{NiO} Zr^{..}_{Ni} + V''_{Ni} + 2O^x_O \qquad [5]$$

$$ZrO_2 \xrightarrow{NiO} Zr^{..}_{Ni} + 2[V''_{Ni} + Ni^{.}_{Ni}] + 2O^x_O \qquad [6]$$
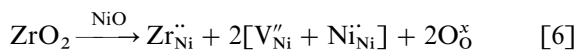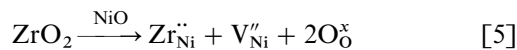
The dilute Zr^{4+} cations could create local domains in which Ni^{3+} should be expelled into interstitial site and thus, in the

vicinity, the 4:1 clusters, the paracrystalline state of defect clusters and then the spinel Ni_3O_4 could precipitate in local domains. The theoretical analysis (6) of 4:1 cluster formation using molecular orbital theory and assuming the dopant Ni^{3+} in the interstitial site, i.e.,

$$6Ni^{..}_{Ni} + 3V''_{Ni} \rightarrow Ni^{...}_i + 4V''_{Ni} + 5Ni^{.}_{Ni}, \qquad [7]$$
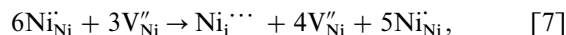
suggests that they are unstable in $Ni_{1-x}O$. However, more recent calculation suggested the 4:1 and 6:2 clusters are energetically favored for $Ni_{1-x}O$ (8).

It is also interesting to consider the presence of oxygen vacancies (i.e., $Zr^{oct}\square_nO_{6-m}\square_m$) in the local domains as in zirconia polymorphs and PSZ studied by X-ray absorption spectroscopy technique using synchrotron light source (46–49) and satellite dark field imaging technique using TEM (50). The charge-compensating oxygen vacancies caused by Y doping are preferentially located next to Zr ions (i.e., ZrO_7), leaving eightfold oxygen coordination for the Y ions (47). The undersized dopants (Fe and Ga), however, were found to compete with Zr ions for the oxygen
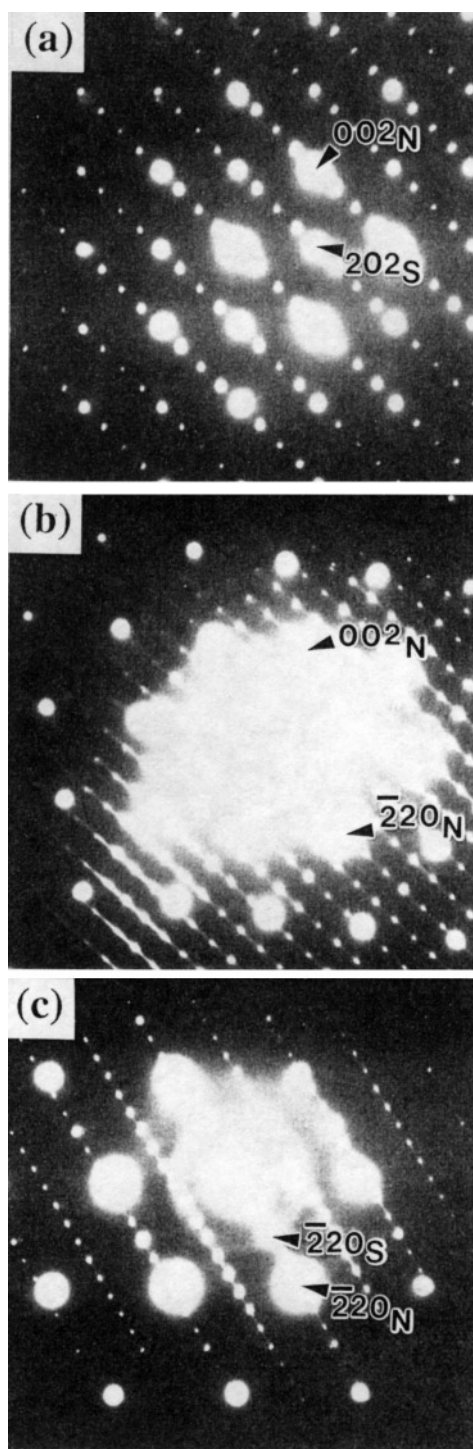
FIG. 9. SAD patterns of a single spinel-derived variant: (a) [010], (b) [110], and (c) [111] zone axes (same specimen as Fig. 6).

vacancies in zirconia, resulting in six-fold oxygen coordination for the dopant and a large disturbance to the surrounding next nearest neighbors (49). The oxygen vacancies in Zr-doped domains should also affect the defect structure and the migration mechanisms of the surrounding $Ni_{1-x}O$.
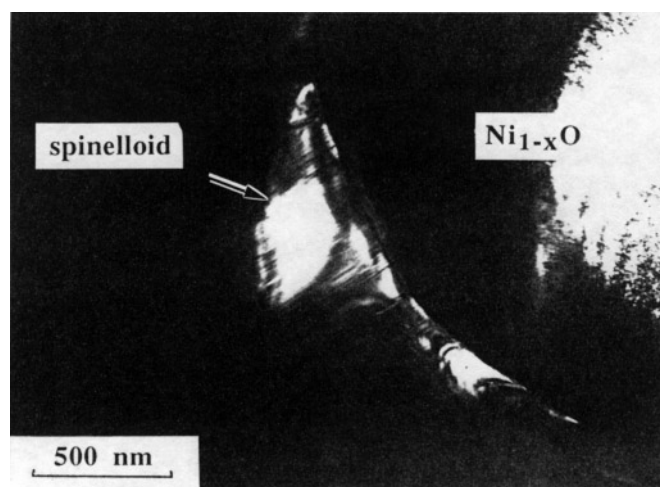

FIG. 10. DFI (use ($\bar{2}20$) spot of spinel) of a spinelloid-containing patch which has ($\bar{1}10$) planar defects edge-on in [111] zone axes (same specimen as Fig. 6).

In this connection, the microanalysis of an oxidized CoO–zirconia (CaO stabilized) eutectic showed that an oxygen gradient exists across the Co_3O_4 spinel with highest levels near the ZrO_2 interface, indicating a rapid diffusion of oxygen in the zirconia lamellae and a slower lateral diffusion into the cobalt oxide to form spinel phase (51).

(c) Dopant Y^{3+}. The Y^{3+} ion, with a larger radius (0.090 nm) than Zr^{4+} (0.072 nm) for coordination number 6 (44), has minor effect on the defect clustering of $Ni_{1-x}O$, because Y^{3+} dissolved much less (ca. 10% of Zr^{4+}) in $Ni_{1-x}O$ either in air or in Ar (34) and the activation energy of diffusion is larger for Y^{3+} (59.8 kcal/mol) than Zr^{4+} (49.0 kcal/mol) (52). (According to Ref. (52), impurity tracer diffusivity of ^{88}Y in NiO single crystal with {100} surface is one order of magnitude smaller than that of ^{95}Zr (e.g. 9.83×10^{-9} cm²/s at 1873 K) over the temperature range of 1273–1873 K in air). Still, the extra doping of Y^{3+} caused significant decrease in the paracrystalline distribution spacing, from $3.5a_o$ to $2.5a_o$ for Zr-doped and (Zr,Y)-codoped $Ni_{1-x}O$, respectively. The substitution of a relatively large Y^{3+} for Ni^{2+} presumably caused a decrease of cluster size and surface energy changes of the clusters analogous to the case of Ca^{2+} substitution for Fe^{2+} in wüstite (53). (The surface energy is principally governed by shearing distortions of the distorted envelopes of the clusters (54).) It is likely that more oxygen vacancies are present in (Zr,Y)-codoped domains, where charge-compensating oxygen vacancies caused by Y-doping are preferentially located next to Zr ions (47). It should be noted also that Zr has very different local structure in the t- and c-solid $ZrO_2–Y_2O_3$ solutions in terms of oxygen-bond distances and coordination number (47). In the t-structure, the first Zr–O shell is bifurcated into two tetrahedra, with outer O ions loosely bound and severely distorted (46).

Thus, possible local structure of t-phase nature is expected to affect oxygen vacancy concentration, and hence defect clustering.

4.3. Energetics of Defect Clustering in Zr-Doped $Ni_{1-x}O$

Previous study of (Zr,Y)-codoped $Ni_{1-x}O$ indicated that the paracrystalline distribution of defects was not formed until aged beyond 100 h at 1573 K in spite of a much earlier saturation of the dopants (29). The present Zr-doped $Ni_{1-x}O$ also remained as rock salt structure when aged at 1573 K for 300 h. Thus the dissolution of Zr^{4+} in a $Ni_{1-x}O$ lattice through Eq. [6] is much rapid than the subsequent formation of defect clusters. In fact, Zr^{4+} diffuses more rapidly and with a smaller activation energy (49.0 kcal/mol) (52) than do smaller Ni^{2+} ion (60.8 kcal/mol) (27). This can be qualitatively understood by a highly polarizable d-electron shell if a larger ion has the expected larger polarizability, i.e., if the larger impurity ion can be more easily squeezed as it passes through the saddle-point configuration (52). Harding (55) also discussed the complex interplay of various terms (migration, correlation, and binding) that arise in the impurity (including Zr) diffusion in nickel oxide; however, the impurity-vacancy binding energy, as in Eq. [6], was not shown. The oversized dopant Zr^{4+} presumably lower the activation energy of Eq. [7] so that Ni^{3+} can be effectively expelled into the interstitial site to form 4:1 clusters.

Analogously to the case of wüstite (4, 13–15), the Ni^{3+} based 4:1 clusters in the Zr^{4+}-doped $Ni_{1-x}O$ may further aggregate as larger units (e.g., the 6:2 cluster composed of two 4:1 clusters with a common edge) which self-assemble as the paracrystalline distribution (16, 17) before transforming into spinel phase. In fact, the binding energies of 4:1 and 6:2 clusters for $Ni_{1-x}O$ have been calculated to be -4.81 and -7.18 eV, respectively, only slightly lower than those (-5.25 and -8.16 eV, respectively) for $Fe_{1-x}O$ (8). For a larger aggregate of clusters, corner sharing could become favored, e.g., the 16:5 cluster with five corner-shared 4:1 clusters (4). It should be noted that the 16:5 cluster is an element of the inverse spinel structure adopted by Fe_3O_4 and could indeed be considered a nucleus of the spinel structure. In fact, computer simulation indicated that a mixture of 13:4 clusters (Koch-Cohen (9)) and 16:5 clusters in the paracrystalline region can provide just the right peak intensity as in the X-ray pattern of quenched $Fe_{1-x}O$ with $x = 0.057$ (17).

In spite of a rather uniform distribution of dopant in the $Ni_{1-x}O$ particle as indicated by EDX analysis, the defect clusters were found to assemble predominantly at interface and dislocations where activation energies for both nucleation and diffusion are low. In this regard, the mobility of Ni vacancies along grain boundaries were indeed found to be greater than in the bulk (56) and the "singly charged" nickel vacancies have a higher binding energy with dislocation than doubly charged vacancies (57). The formation of a spinel-derived phase at the $Ni_{1-x}O$/Y-PSZ interface can be further attributed to solute (in particular Zr^{4+}) segregation, which creates more charge-compensating defects for pronounced clustering.

4.4. Spinelloid Structure

Based on the SAD patterns, the r.p.l. of the spinel derivative is constructed in Fig. 11. The r.p.l. can be indexed as a spinelloid phase, but different from the orthorhombic type found in sintered Y-PSZ-Ni_2AlTi cermet (58). The present type of spinelloid has a B-centered monoclinic (designated as "msp") r.p.l. with a specified crystallographic relationship with the $Ni_{1-x}O$ phase: $[100]_{msp}//[100]_N$, $[001]_{msp}//[\bar{1}10]_{msp}$, and $[010]_{msp}//[001]_N$. Given this crystallographic relationship, spinelloid variants are derived.

The planar defects of this msp phase has the same habit plane $\{110\}_N$ as that for spinelloid in the Y-PSZ-Ni_2AlTi cermet (58), implying a regular arrangement of basic structural units along the $[110]_N$ direction, as for spinelloids I and III in the NiO–Al_2O_3–SiO_2 system at high pressure (59). In spinelloids I and III, there are one-dimensional
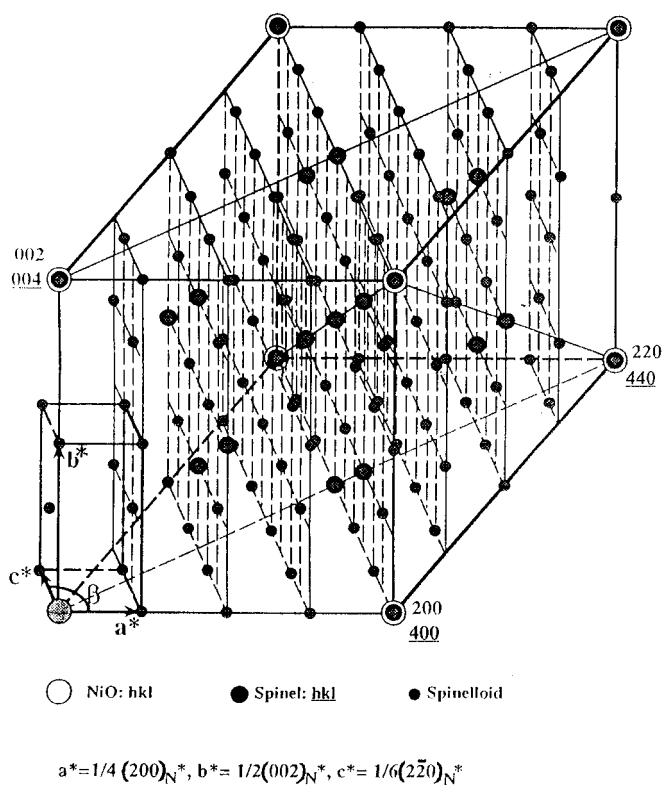

$a^* = 1/4 (200)_N^*,\ b^* = 1/2(002)_N^*,\ c^* = 1/6(2\bar{2}0)_N^*$

FIG. 11. Reciprocal lattice of the spinel-derived phase based on the SAD patterns in Fig. 9.

arrangement of units along the **b** axis as ↑↑↑↓ and ↑↑↓↓, respectively, and the parts with mutually opposite directions of the structural units like ↑↓ are "spinel-type parts" (59). In fact, the {110} type anti-phase domain boundaries in the spinel phase are also of spinelloid nature (31, 60). Further study is required to clarify how the relatively high level of Zr-dopant with charge- and volume-compensating nickel and oxygen vacancies caused the formation of the spinelloid phase. It also remains to be clarified if the wavelike nature of the spinel phase formed in the early stage of aging (Fig. 4b) is analogous to paracrystalline state of $Ni_{1-x}O$ or due to crystallographic shear as for iron-doped TiO_2 (rutile) (61).

5. SUMMARY

1. The defect clustering and ordering of Zr- or (Zr,Y)-doped $Ni_{1-x}O$ were much easier at a higher annealing temperature (1873 vs 1573 K) and preferred to occur at interfaces and dislocations than in the bulk.

2. The predominantly dissolved Zr^{4+} cations, in octahedral sites with charge- and volume-compensating nickel and oxygen vacancies (i.e., $Zr^{oct}\square_nO_{6-m}\square_m$), could create local domains in which Ni^{3+} should be expelled, and thus, in the vicinity the paracrystalline state and then the spinel Ni_3O_4 could precipitate in local domains.

3. The spacing of paracrystalline distribution is 2.5 and 3.5 times the lattice parameter for (Zr,Y)-codoped and Zr-doped $Ni_{1-x}O$, respectively.

4. The spinelloid, a spinel derivative structure with planar defects parallel to a specific {110} plane of spinel, was formed for the $Ni_{1-x}O$ particles located at Y-PSZ grain boundaries. The spinelloid can be tentatively indexed as a B-centered monoclinic cell in the reciprocal space.

ACKNOWLEDGMENT

REFERENCES

1. L. S. Darken and R. W. Gurry, *J. Am. Chem. Soc.* **68,** 798 (1946).
2. W. L. Roth, *Acta Crystallogr.* **13,** 140 (1960).
3. N. N. Greenwood and A. T. Howe, *J. Chem. Soc., Dalton Trans.* 110 (1972).
4. C. R. A. Catlow and B. E. F. Fender, *J. Phys. C: Solid State Phys.* **8,** 3267 (1975).
5. A. B. Anderson, R. W. Grimes, and A. H. Heuer, *J. Solid State Chem.* **55,** 353 (1984).
6. R. W. Grime, A. B. Anderson, and A. H. Heuer, *J. Am. Ceram. Soc.* **69,** 619 (1986).
7. M. R. Press and D. E. Ellis, *Phys. Rev. B* **35,** 4438 (1987).
8. S. M. Tomlinson, C. R. A. Catlow, and J. H. Harding, *J. Phys. Chem. Solids* **51,** 479 (1990).
9. F. B. Koch and J. B. Cohen, *Acta Crystallogr. B* **25,** 275 (1969).
10. J. R. Gavarri, C. Carel, and D. Weigel, *J. Solid State Chem.* **29,** 81 (1979).
11. M. J. Radler, J. B. Cohen, and J. Faber, *J. Phys. Chem. Solids,* **51,** 217 (1990).
12. W. Schweika, A. Hoser, M. Martin, and A. E. Carlsson, *Phys. Rev. B* **51,** 15771 (1995).
13. P. Vallet and P. Raccah, *Mem. Sci. Rev. Metall.* **62,** 1 (1965).
14. B. Andersson and J. O. Sletnes, *Acta Crystallogr., Sect. A* **33,** 268 (1977).
15. J. Manenc, J. Bourgeot, and J. Benard, *C. R. Acad. Sci. Paris* **258,** 4528 (1964).
16. T. R. Welberry and A. G. Christy, *J. Solid State Chem.* **117,** 398 (1995).
17. T. R. Welberry and A. G. Christy, *Phys. Chem. Minerals* **24,** 24 (1997).
18. S. Iijima, *in* "The Nature of Extended Defects in Crystals," Vol. 2, p. 217. Australian Academy of Science, Canberra, Australia, 1974.
19. T. Ishiguro and S. Nagakura, *Electron Microsc., 11th Proc. Int. Congr.,* 963 (1986).
20. A. Yamamoto, *Acta Crystallogr., Sect. B* **38,** 1451 (1982).
21. G. Nihoul, J. R. Gavarri, and C. Carel, *Acta Crystallogr., Sect. B* **47,** 333 (1991).
22. H. G. Sockel and H. Schmalzried, *Ber. Bunsenges. Phys. Chem.* **72,** 745 (1968).
23. C. R. A. Catlow and A. M. Stoneham, *J. Am. Ceram. Soc.* **64,** 234 (1981).
24. C. M. Osburn and R. W. Vest, *J. Phys. Chem. Solids* **32,** 1331 (1971).
25. R. L. Lalauze and J. H. Meunier, *Oxid. Met.* **12,** 183 (1978).
26. W. C. Tripp and N. M. Tallan, *J. Am. Ceram. Soc.* **53,** 531 (1970).
27. M. L. Volpe and J. Reddy, *J. Chem. Phys.* **53,** 1117 (1970).
28. J. Szuber, *J. Mater. Sci.* **19,** 1991 (1984).
29. P. Shen, S. Chen, and H. S. Liu, *Mater. Sci. Eng. A* **161,** 135 (1993).
30. D. B. Williams, "Practical Analytical Electron Microscopy in Materials Science," p. 157. Philips Electronic Instruments, Inc., Electron Optics Publishing Group, Mahwah, NJ, 1984.
31. S. R. Wang and P. Shen, *J. Solid State Chem.* (in press).
32. G. Remaut, P. Delavignette, A. Lagasse, and S. Amelinckx, *Phys. Stat. Sol.* **11,** 329 (1965).
33. J. Chen and P. Shen, *Scr. Mater.* **37,** 1287 (1997).
34. E. N. Timofeeva, N. I. Timofeeva, L. N. Drozdova, and O. A. Mordovin, 1*zv. Akad. Nauk SSSR, Neorg. Mater.* **5,** 1155 (1969).
35. V. P. Dravid, C. E. Lyman, M. R. Notis, and A. Revcolevschi, *Metall. Trans. A* **21,** 2309 (1990).
36. P. Kofstad, "Nonstoichiometry, Diffusion and Electrical Conductivity in Binary Metal Oxides." Wiley Interscience, New York, 1972.
37. A. Atkinson, A. E. Hughes, and A. Hammou, *Phil. Mag. A* **43,** 1071 (1981).
38. F. A. Kröger and H. J. Vink, *Solid State Phys.* **3,** 307 (1956).
39. N. L. Peterson and C. L. Wiley, *J. Phys. Chem. Solids* **46,** 43 (1985).
40. R. W. Grime, A. B. Anderson, and A. H. Heuer, *J. Phys. Chem. Solids* **48,** 45 (1987).
41. D. M. Duffy, *Phil. Mag.* **50,** 143 (1984).
42. C. Gleitzer, J. Nowothy, and M. Rekas, *Apply. Phys. A* **53,** 310 (1991).
43. J. Nowothy and I. Sikora, *J. Am. Ceram. Soc.* **65,** 192 (1982).
44. R. D. Shannon, *Acta Crystallogr., Sect. A* **32,** 751 (1976).
45. S. Chen and P. Shen, *Mater. Sci. Eng. A* **114,** 159 (1989).
46. P. Li, I. W. Chen, and J. E. Penner-Hahn, *Phys. Rev. B* **48,** 10063 (1993).
47. P. Li, I. W. Chen, and J. E. Penner-Hahn, *Phys. Rev. B* **48,** 10074 (1993).
48. P. Li, I. W. Chen, and J. E. Penner-Hahn, *Phys. Rev. B* **48,** 10082 (1993),
49. P. Li, I. W. Chen, and J. E. Penner-Hahn, *J. Am. Ceram. Soc.* **77,** 118 (1994).
50. R. L. Withers, J. G. Thompson, N. Gabbitas, L. R. Wallenberg, and T. R. Welberry, *J. Solid State Chem.* **120,** 290 (1995).
51. J. Bentley, S. McKernan, C. B. Carter, and A. Revcolevschi, Inst. Phys. Conf. Ser. No 138: Section 2, "Electron Microscopy and Analysis," p. 39. IOP Publishing, Bristol, UK, 1993.
52. K. Hoshino and N. L. Peterson, *J. Phys. Chem. Solids* **45,** 963 (1984).
53. C. Carel and J. R. Gavarri, *J. Phys. Chem. Solids* **51,** 1131 (1990).
54. J. R. Gavarri and C. Carel, *Phase Transition* **14,** 103 (1989).

55. J. H. Harding, *in* "Advances in Ceramics, Vol. 23, Nonstoichiometric Compounds," C. R. A. Catlow and W. C. Mackrodt (eds.), p. 229. The American Ceramic Society, Westerville, OH, 1987.
56. A. Atkinson and R. I. Taylor, *Phil. Mag. A* **43,** 979 (1981).
57. J. Rabier, J. Soullard, and M. P. Puls, *Phil. Mag. A* **61,** 99 (1990).
58. P. T. Chao, P. Shen, and S. L. Hwang, *Mater. Sci. Eng A* **112,** 233 (1989).

59. H. Horiuchi, M. Akaogi, and H. Sawamoto, *in* "Advances in Earth and Planetary Sciences 12, High-Pressure Research in Geophysics" (A. Akimoto and M. H. Manghnani, eds.), pp. 391–403 and literature cited therein. Center for Academic Publications, Tokyo, 1982.
60. G. D. Price, *Phys. Chem. Minerals* **10,** 77 (1983).
61. L. A. Bursill, D. J. Netherway, and I. E. Grey, *Nature* **272,** 405 (1978).